such a transition not been observed previously in ^{4}He-II? A number of reasons can be listed: (1) in ^{3}He the viscosity of the normal fraction is four orders of magnitude higher. Thus there is no ambiguity about the state of the normal component, unlike in the case of ^{4}He-II. (2) The vortex-core radius in ^{3}He-B exceeds by two orders of magnitude that in ^{4}He-II, where it is only of atomic size. Therefore vortex pinning and remanence at solid walls can often be neglected in ^{3}He-B and metastable states with high-velocity superflow become possible. (3) The most important difference lies in the value of mutual friction. In ^{4}He-II the dissipative part α is small and influences vortex motion relatively little. Only within a narrow temperature interval $\Delta T/T_\lambda \approx 2 \times 10^{-3}$ from T_λ one finds $q > 1$ and expects different behaviour. No conclusive measurements exist from so close to T_λ.

To conclude we may now predict that in helium superfluids the transition at $q_c \approx 1$ lies close to T_λ in ^{4}He-II, in the middle of the experimentally accessible temperature range in ^{3}He-B, and below that at extremely low temperatures in ^{3}He-A. This prediction is consistent with presently available experimental information. Perhaps in other hydrodynamic systems, which consist of two or more components, superfluid or viscous, the stability of turbulence might also be governed by an intrinsic parameter, in addition to the Reynolds number. □

Methods

Vortex injection

We use four different injection methods: (1) vortex loops are created at a rough spot on the cylindrical sample boundary by increasing Ω to the critical value Ω_c (ref. 9). (2) In neutron irradiation, vortices are created via the heat release from neutron capture reactions[10]. (3) Vortex loops may leak through the small orifice which connects the NMR sample to the rest of the liquid ^{3}He volume[12]. (4) The most efficient method is to use an instability of the phase boundary between the ^{3}He-A and ^{3}He-B phases in rotation[7]. The AB boundary can be stabilized to a fixed location in a suitable magnetic field gradient. This technique has been employed to collect the data in Fig. 3, to fill the (Ω, T) plane with a dense grid of measurements. The instability of the AB interface produces a small random number ($\Delta N \approx 10$) of B-phase vortex loops of which one end sticks out of the AB interface while the other end travels along the cylindrical sample boundary during the expansion process into rectilinear vortices[7]. The four injection processes have different temperature-dependent critical velocities $\Omega_c(T)$, which are continuous at $0.60T_c$ and consistently display the transition from regular to turbulent dynamics at $0.60T_c$.

NMR signatures from turbulence

The lowest measured critical velocities are about 0.5 rad s^{-1} at $T \lesssim 0.50T_c$. Even at these velocities (Re$_s \lesssim 70$) the injection leads only to turbulent loop expansion. The axial expansion of the vorticity along the $\hat{\Omega}$ axis between the two signal coils is found to be controlled by the mutual-friction damping α: the time of expansion τ across a vertical d agrees with the expression $\tau = d/(\alpha\Omega R)$. The extracted $\alpha(T)$ reproduces the result of ref. 6, is continuous across the transition at $0.60T_c$, and is thus indifferent to whether the vorticity moves as noninteracting loops or as a network of loops. Below the transition at $0.60T_c$ the vortex tangle is observed to decay with a time constant of around 30 s which decreases towards lower temperatures. This we interpret to indicate that reconnection processes are primarily responsible for the decay rather than the mutual-friction dominated expansion of individual loops.

Simulation

We use the vortex filament model[13,14] in the rotating frame[15]. A vortex is represented in parametric form by $\mathbf{s} = \mathbf{s}(\xi, t)$, where $\mathbf{s}$ refers to a point on the filament and ξ is the arc length along it. The spatial and time evolutions are integrated rigorously using the Biot–Savart law. The vortex velocity $\dot{\mathbf{s}}$ is calculated from the dynamic equation $\dot{\mathbf{s}} = \mathbf{v}_{sl} + \alpha' \mathbf{s}' \times [\mathbf{s}' \times \mathbf{v}_{sl}] - \alpha(\mathbf{s}' \times \mathbf{v}_{sl})$ (recall that $\mathbf{v}_n = 0$), where the local superfluid velocity $\mathbf{v}_{sl}$ includes all contributions to the superflow at $\mathbf{s}(\xi, t)$. As boundary conditions we use smooth solid-walls with image vortices.

Analytic approach

Equation (2) is a first-order differential equation in contrast to the second order Navier–Stokes equation (1) of conventional hydrodynamics. Our result suggests a new approach to classical turbulence: when the vorticity is modelled with stable vortex filaments, their dynamics can be derived from a first-order equation by introducing an effective vortex-filament viscosity.

1. Vinen, W. F. & Niemela, J. J. Quantum turbulence. *J. Low-Temp. Phys.* **128,** 167–231 (2002).
2. McComb, W. D. *The Physics of Fluid Turbulence* 2 (Clarendon, Oxford, 1990).
3. Sonin, E. B. Vortex oscillations and hydrodynamics of rotating superfluids. *Rev. Mod. Phys.* **59,** 87–155 (1987).
4. Barenghi, C. F. *et al.* Thermal excitation of waves on quantized vortices. *Phys. Fluids* **28,** 498–504 (1985).
5. Kopnin, N. B. *Theory of Nonequilibrium Superconductivity* 271 (Clarendon, Oxford, 2001).
6. Bevan, T. D. C. *et al.* Vortex mutual friction in superfluid ^{3}He. *J. Low-Temp. Phys.* **109,** 423–459 (1997).
7. Blaauwgeers, R. *et al.* Shear flow and Kelvin-Helmholtz instability in superfluids. *Phys. Rev. Lett.* **89,** 155301 (2002).
8. Ostermeier, R. M. & Glaberson, W. I. Instability of vortex lines in the presence of axial normal fluid flow. *J. Low-Temp. Phys.* **21,** 191–196 (1975).
9. Ruutu, V. M. H. *et al.* Intrinsic and extrinsic mechanisms of vortex formation in superfluid ^{3}He-B. *J. Low-Temp. Phys.* **107,** 93–164 (1997).
10. Ruutu, V. M. H. *et al.* Vortex formation in neutron-irradiated superfluid ^{3}He as an analogue of cosmological defect formation. *Nature* **382,** 334–336 (1996).
11. Fisher, S. N. *et al.* Generation and detection of quantum turbulence in superfluid ^{3}He-B. *Phys. Rev. Lett.* **86,** 244–247 (2001).
12. Skrbek, L. *et al.* Vortex flow in rotating superfluid ^{3}He-B. *Physica B* **329–333,** 106–107 (2003).
13. Schwarz, K. W. Three-dimensional vortex dynamics in superfluid ^{4}He: Homogenous superfluid turbulence. *Phys. Rev. B* **38,** 2398–2417 (1988).
14. Tsubota, M. *et al.* Dynamics of vortex tangle without mutual friction in superfluid ^{4}He. *Phys. Rev. B* **62,** 11751–11762 (2000).
15. Tsubota, M. *et al.* Rotating superfluid turbulence. *Phys. Rev. Lett.* **90,** 205301 (2003).

··

Water-driven structure transformation in nanoparticles at room temperature

Hengzhong Zhang*, **Benjamin Gilbert***, **Feng Huang & Jillian F. Banfield**

Department of Earth and Planetary Sciences, University of California, Berkeley, California 94720, USA

* These authors contributed equally to this work

The thermodynamic behaviour of small particles differs from that of the bulk material by the free energy term γA—the product of the surface (or interfacial) free energy and the surface (or interfacial) area. When the surfaces of polymorphs of the same material possess different interfacial free energies, a change in phase stability can occur with decreasing particle size[1,2]. Here we describe a nanoparticle system that undergoes structural changes in response to changes in the surface environment rather than particle size. ZnS nanoparticles (average diameter 3 nm) were synthesized in methanol and found to exhibit a reversible structural transformation accompanying methanol desorption, indicating that the particles readily adopt minimum energy structural configurations[3,4]. The binding of water to the as-formed particles at room temperature leads to a dramatic structural modification, significantly reducing distortions of the surface and interior to generate a structure close to that of sphalerite (tetrahedrally coordinated cubic ZnS). These findings suggest a route for post-synthesis control of nanoparticle structure and the potential use of the nanoparticle structural state as an environmental sensor. Furthermore, the results imply that the structure and reactivity of nanoparticles at planetary surfaces, in interplanetary dust[5] and in the biosphere[6,7], will depend on both particle size and the nature of the surrounding molecules.

ZnS belongs to a class of important II–VI semiconductors that includes CdS and CdSe. Cadmium chalcogenides are often synthesized as nanoparticles for studies of size-dependent phenomena,
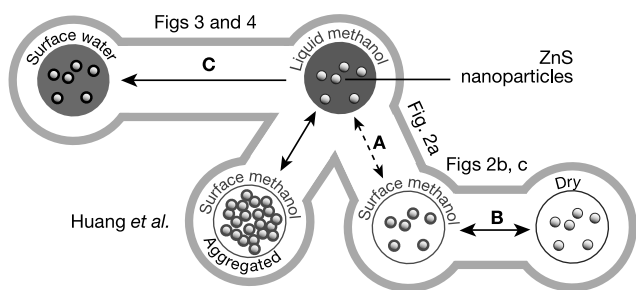
Figure 1 Diagram showing the experiments (A, B and C) performed in this and related work[3,4]. The dashed double-headed arrow indicates a reversible step with no structural change; solid double-headed arrows indicate cases where nanoparticle's surface environment causes reversible structural modification. The single-headed arrow indicates that the water-driven transformation has not been reversed, probably owing to strong chemisorption of the water at the nanoparticle surface.

Figure 3 The effect of water binding on the structure and size of uncapped ZnS nanoparticles in methanol. See step C in Fig. 1. **a**, Conventional XRD reveals a dramatic increase in crystallinity after addition of water, as the 220 and 311 reflections become resolved. Low angle diffraction from the methanol solvent ("Me") interferes with the 111 peak; 'Ref.' indicates 20 nm ZnS (mostly sphalerite, commercial, Aldrich). **b**, UV–vis. absorption spectroscopy shows no change in the onset of absorption, indicating that no coarsening occurs due to water addition. Solid line, sample in methanol; dotted line, following addition of water. The vertical bar indicates the absorption threshold position for bulk sphalerite ZnS (see Supplementary Fig. 1).

such as quantum confinement[8]. In CdSe, changes in size correlate with changes in colour that span the visible (vis.) spectrum[9,10], while confinement effects in ZnS appear in the ultraviolet (UV) region[11]. Here we integrate structure modelling and materials characterization methods to demonstrate the ways in which ZnS nanoparticle structure responds to changes in the surface environment. The experimental framework is shown in Fig. 1.

Nanocrystalline ZnS was synthesized in anhydrous methanol without a surfactant. The average particle diameter determined from the edge position of the UV–vis. absorption threshold is 2.8 ± 0.2 nm, and when determined by transmission electron microscopy (TEM) is 3.0 ± 0.3 nm (Supplementary Figs 1 and 2). If the nanoparticle size is determined by X-ray diffraction (XRD) using the Scherrer equation[12], which only considers size contributions to peak broadening, the estimated diameter is 1.4 nm. The discrepancy implies that significant strain is present within the nanoparticles.

We demonstrated that the ZnS nanoparticles are not trapped in a metastable initial state but can undergo reversible structural transformations at room temperature. For example, Huang et al.[3,4] showed that when particles are ultrasonically disaggregated at room temperature and allowed to reaggregate, a reversible structural transformation occurs. In addition, we tested for reversible

structural transformations accompanying removal and resorption of methanol.

Methanol-suspended ZnS nanoparticles were transferred to vacuum at room temperature. Liquid methanol rapidly evaporated, but XRD of the ZnS nanoparticles showed no structural change (Fig. 2a). Thermal desorption measurements revealed that methanol was retained on the nanoparticle surface and was evolved above 50 °C (Supplementary Information). Extended X-ray absorption fine structure (EXAFS) measurements showed that after thermal desorption of methanol at 50 °C the nanoparticles are structurally distinct from those in the presence of methanol. EXAFS data indicated that the nanoparticles transform from a distorted four-coordinate structure (in methanol) to an unidentified phase (dry) (Supplementary Table 1 and Supplementary Fig. 3). The real-space EXAFS correlation functions indicated that the original structure was regained after readdition of methanol (Fig. 2b, c). Thus, the experiment demonstrates a reversible structural transformation associated with methanol desorption and replacement.

To study the effect of water addition, 50 μl water per ml methanol was added to the nanocrystalline ZnS in liquid methanol, and the sample characterized in situ (no drying). Figure 3a and b shows XRD patterns and UV–vis. spectra of the nanocrystalline ZnS in methanol without water, and 24 h after addition of water. The XRD
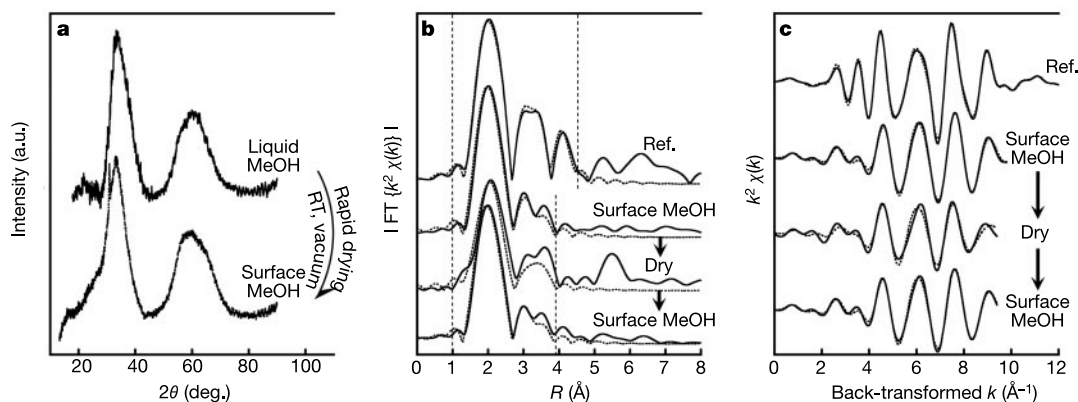
Figure 2 A reversible structural change associated with methanol desorption. **a**, In situ X-ray diffraction of ZnS nanoparticles shows that rapid pre-drying (step A in Fig. 1) does not induce structure change. When surface methanol (MeOH) is removed by thermal desorption at 50 °C (step B, Fig. 1) the EXAFS data (**b**, Fourier transforms (FT) of k^2 weighted $\chi(k)$ EXAFS functions, **c**, back transformed data) indicate a structural

modification that can be reversed by readdition of methanol. EXAFS spectra labelled "Ref." are from bulk ZnS (sphalerite). The vertical dashed lines are the real-space fitting ranges (three-shells for the reference, two-shells for nanoparticles). Data and fits are given by solid and dotted curves, respectively.
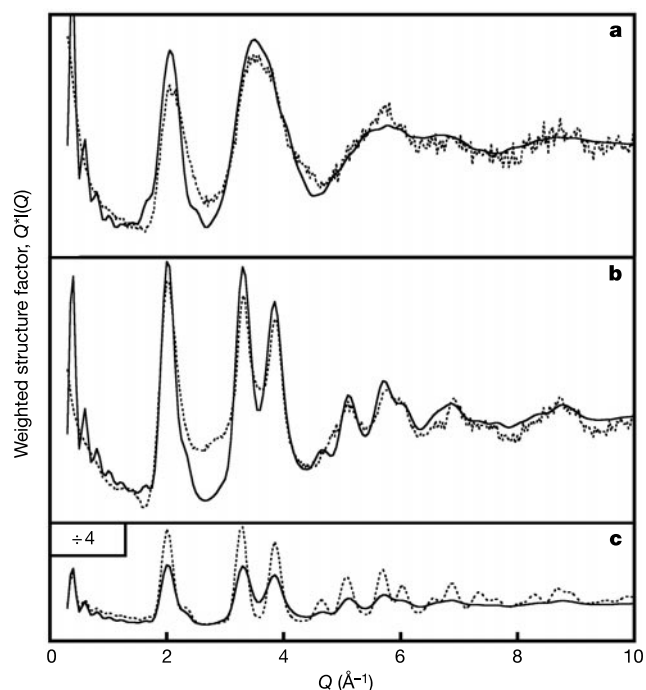
Figure 4 Wide-angle X-ray scattering (WAXS) observation of water binding. Experimental (dotted lines) WAXS Q-weighted structure factors of ZnS nanoparticles in methanol **a**, before and **b**, after water binding (step C in Fig. 1). Superimposed (solid lines) are the patterns predicted by molecular dynamics (MD) relaxation of a 3 nm ZnS particle **a**, without and **b**, with surface bound water. The methanol background has been subtracted from the experimental data. **c**, The WAXS pattern from the 3 nm MD simulation in the presence of water (solid line) is compared with the pattern of an unrelaxed 3 nm spherical fragment of the sphalerite structure (dotted line).

patterns clearly demonstrate structural change. However, the UV–vis. absorption threshold position is unchanged, indicating that no significant size change occurs following water addition (Fig. 3b). TEM imaging of nanoparticles without water, and following the addition of water, also revealed no size change (Supplementary Fig. 2). Peak positions in the XRD spectrum following water addition suggest that the disordered structure undergoes a transformation to more crystalline sphalerite-like structure.

The water-driven structure transformation in ZnS was further studied with synchrotron-based wide angle X-ray scattering (WAXS) to achieve higher quality *in situ* diffraction measurements to high $Q = (4\pi\sin\theta)/\lambda$ with accurate background subtraction, and to obtain the real-space pair correlation function $G(r)$ (Supplementary Fig. 4). From the conventional XRD data in Fig. 3 and the WAXS data in Fig. 4 we conclude that nanocrystalline ZnS in methanol undergoes a room temperature structural modification, best characterized as a disorder-to-order transition, following water binding. Identical structural behaviour was observed with *in situ* X-ray absorption near edge structure (XANES) and EXAFS spectroscopies (Supplementary Figs 5a, b).

Further insight into the initial and final structures and into the transition itself are obtained by molecular dynamics (MD) simulations of model particles of different sizes (2.0, 2.5, 3.0, 4.0 and 5.0 nm), from different initial structures (tetrahedrally coordinated hexagonal (wurtzite) or cubic (sphalerite) ZnS), and with different water coverages (1, 3 and 5 H_2O molecules per nm^2 ZnS surface). The MD simulations were performed with a time step of 5×10^{-4} ps (up to 100 ps or more MD time) until a full relaxation of the initial configuration was achieved without loss of the original phase (see Methods).

We calculated the theoretical WAXS pattern associated with each final MD structure. The experimental trend towards increased crystallinity following water binding was reproduced by the MD series. The closest agreement with data from nanoparticles in
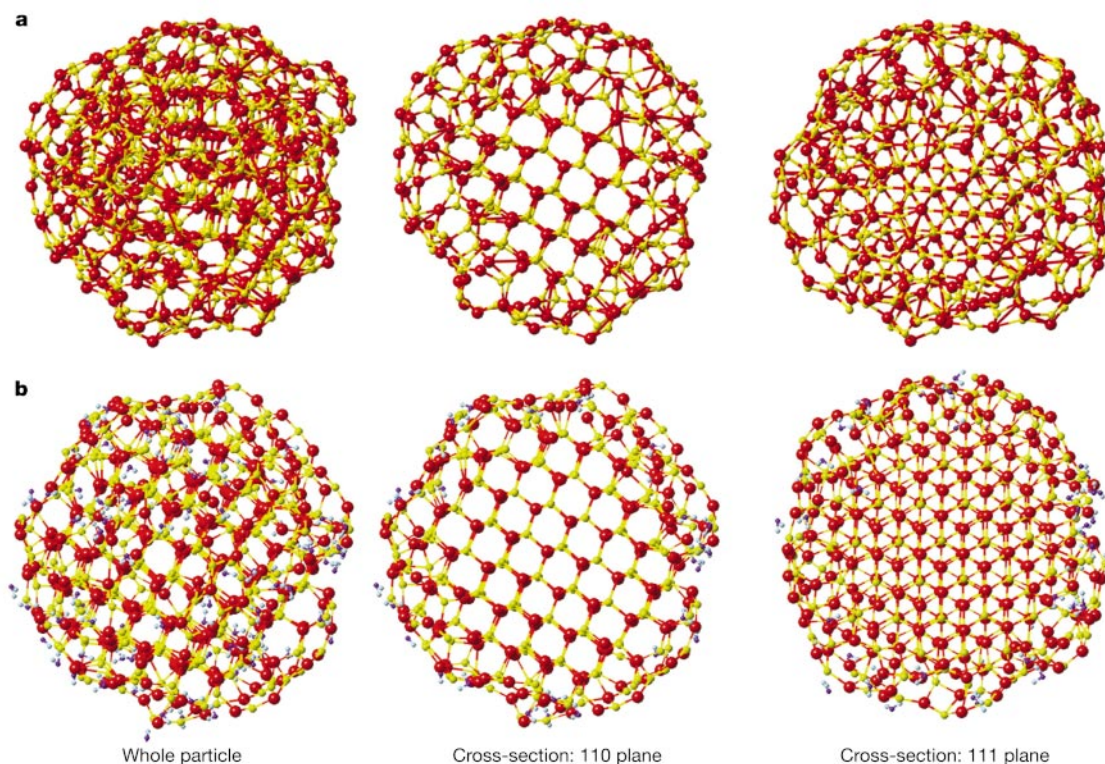
Figure 5 Molecular dynamics predictions of the structure of a 3 nm ZnS nanoparticle. **a**, Without surface-bound water, and **b**, with surface-bound water. S atoms yellow, Zn red, O blue, H light blue. Central cross-sections through the particles give a clearer picture of internal structure. Regular interior (110) and (111) planes are evident in both structures, but in the absence of water ligands the outer shell is severely distorted.

methanol was obtained from MD relaxation of an unpassivated 3 nm sphalerite nanocrystal. MD relaxation of 2.5 and 3 nm ZnS nanocrystals (with water coverage at 3 H_2O molecules per nm^2) both gave close agreement with data in the presence of water. In each case, the MD particle size is close to the actual nanoparticle size. MD simulations of particles that were not close in size to the experimental nanoparticles gave poor fits to the data. The corresponding theoretical WAXS patterns are displayed in Fig. 4, and views of the nanoparticle structures are given in Fig. 5.

The experimental X-ray scattering data and MD calculations indicate a highly disordered structure within the ZnS nanoparticles in methanol. However, cross-section views through the MD structure (Fig. 5) reveal a crystalline central core, indicating that the surfaces of unpassivated nanoparticles undergo reconstruction that is more extreme and penetrates deeper than that documented previously at macroscopic surfaces[13] and step edges[14]. Simulations suggest that distortions due to the cumulative effects of bounding surfaces in three dimensions affect at least four atomic layers, approximately 0.8 nm. Analogous distortion has been inferred from studies of cold noble gas clusters[15,16], but not in covalently bonded solids.

We also attempted to model the WAXS data using fragments of perfect sphalerite or wurtzite that contained stacking faults and thermal and structural disorder. None of these models generated fits to the data that were as good as those from MD simulations. This finding is significant, as perfect structures are frequently the starting point for calculations of nanoparticle properties[17–19]. The existence of surface relaxation and reconstruction has been proposed on the basis of theoretical[20,21] and experimental studies[22,23], but no previous study has obtained agreement between structural data and simulations that include interfacial interactions.

The MD simulations show that interactions between water and ZnS decrease the interfacial energy. The resulting increase in crystallinity propagates through the nanoparticle, driven in the simulation by kinetic energy obtained from the isothermal environment. The low water coverage required to increase the crystallinity in the MD simulations indicates a strong water interaction with the surface, consistent with the surface chemistry of hydrated ZnS (ref. 24). The enthalpy change associated with water adsorption was estimated from the MD simulations to be $\sim$500 kJ per mol H_2O at 3 H_2O per nm^2 ZnS surface coverage, but includes both the heat of adsorption plus structural stabilization energy. By comparison, the calorimetrically determined heat of water adsorption for nanocrystalline alumina is 250–300 kJ per mol H_2O at 3 H_2O per nm^2 Al_2O_3 surface coverage[1]. The MD prediction for nanocrystalline ZnS therefore indicates both strong interaction between water and the surface, and a very large stabilization effect. The MD simulations predict that the polar water molecules orient to permit hydrogen and oxygen bonding to the terminating S and Zn ions. Surface interactions with methanol (not included here) are presumably weaker owing to its lower molecular polarity.

Although a more crystalline structure is obtained when water interacts with the nanoparticle, inspection of the surface structure shows residual surface strain, in agreement with prior EXAFS analyses of covalently capped CdTe nanoparticles[25]. Comparison of theoretical WAXS patterns for relaxed and unrelaxed 3 nm particles (Fig. 4c) shows that the structure also retains disorder relative to perfect sphalerite. □

Methods

Nanoparticle synthesis and transformation

3 nm ZnS nanoparticles were synthesized in anhydrous methanol by dropwise addition of 1 M $ZnCl_2$ to 1 M Na_2S under a N_2 atmosphere at room temperature. The resulting suspension was washed three times and stored in methanol. Two 1.9 ml aliquots of the homogenous product were removed, and 100 µl H_2O or methanol added. Size and structure analyses were performed 24 h later on both samples.

X-ray diffraction

A Bruker D8 Discover GADDS diffractometer operated in the reflective geometry with Co K_α radiation ($\lambda = 1.790$ Å) was used to measure dilute suspensions of ZnS nanoparticles in methanol in a low background quartz wet-cell with a thin Kapton window in a flat plate geometry.

UV–vis. spectroscopy

UV–vis. absorption spectra were acquired with an Agilent 8453 spectrophotometer, from synthesized and transformed ZnS nanoparticles in methanol following 4:1 dilution.

WAXS

WAXS was performed on the 11-ID-C beamline of the Advanced Photon Source, Argonne, Illinois, with X-ray wavelength $\lambda = 0.10759$ Å. Suspensions of ZnS nanoparticles were placed in cylindrical plastic containers (diameter 7 mm, beam path 6.5 mm) with Kapton entrance and exit windows. No signal from water ($g(OH)$ or $g(OO)$) was observed in the real space or reciprocal WAXS patterns[26]. Theoretical calculations of WAXS intensity were derived from the atomic coordinates of models of the nanocrystals using the Debye equation, incorporating a fitted Debye Waller factor[27]:

$$I(Q) = \sum_i \sum_j f_i f_j \frac{\sin(Qr_{ij})}{Qr_{ij}} \exp[-2M]$$

MD simulations

Zinc sulphide was described using a shell model, designed to account for molecular polarity, with a Buckingham form of the pair-wise interactomic potential functions, plus an angle-bending form of the three-body interaction between nearest neighbour S–Zn–S atoms[28]. Using this description of ZnS, at 300 K the predicted lattice parameters of the bulk sphalerite, wurtzite and the rock-salt phases of ZnS are, respectively, no more than 0.1%, 2.8% and 0.3% different from the literature values. The predicted transition pressure from sphalerite to rock-salt phase at 300 K is 12 GPa, consistent with ref. 29. In the evaluation of three water models, the shell model[30] showed best compatibility with the ZnS potentials, and was selected over the simple point charge SPCE[31] and central force CF[32] models. The short range Zn–O and S–H interactions also assume a Buckingham potential function, the former taken from ref. 33, the latter obtained from a fit to first principles data for the ground state H–HS potential well in gas phase H_2S (ref. 34).

$$u_{S-H}(\text{short-range}) = 15,644.3\exp\left(-\frac{R_{S-H}}{0.1565}\right) - \frac{21.289}{R_{S-H}^6},$$

where u is in eV and R in Å. The MD simulations were run in a canonical assemble at 300 K using a Nose–Hoover algorithm, or (optionally, at large times) a gaussian algorithm, with a time step of 0.5 fs for no less than 100 ps.

1. McHale, J. M., Auroux, A., Perotta, A. J. & Navrotsky, A. Surface energies and thermodynamic phase stability on nanocrystalline aluminas. *Science* **277,** 788–791 (1997).
2. Zhang, H. & Banfield, J. F. Thermodynamic analysis of phase stability of nanocrystalline titania. *J. Mater. Chem* **8,** 2073–2076 (1998).
3. Huang, F., Zhang, H., Gilbert, B. & Banfield, J. F. Surface state controlled nanocrystalline ZnS structure transformation. *Abstr. Pap. Am. Chem. Soc.* **225,** 431-Phys (2003).
4. Huang, F., Zhang, H., Gilbert, B. & Banfield, J. F. Reversible, surface-controlled structure transformation in nanoparticles induced by aggregation-disaggregation. *Phys. Rev. Lett.* (submitted).
5. Li, A. & Draine, B. T. Are silicon nanoparticles an interstellar dust component? *Astrophys. J.* **564,** 803–812 (2002).
6. Labrenz, M. *et al.* Formation of sphalerite (ZhS) deposits in natural biofilms of sulphate-reducing bacteria. *Science* **270,** 1744–1747 (2000).
7. Banfield, J. F. & Navrotsky, A. (eds) *Nanoparticles and the Environment* (Reviews in Mineralogy and Geochemistry, Vol. 44, Mineralogical Society of America, Washington, 2001).
8. Alivisatos, A. P. Perspectives on the physical chemistry of semiconductor nanocrystals. *J. Phys. Chem.* **100,** 13226–13239 (1996).
9. Bruchez, M. Jr, Moronne, M., Gin, P., Weiss, S. & Alivisatos, A. P. Semiconductor nanocrystals as fluorescent biological labels. *Science* **281,** 2013–2016 (1998).
10. Murray, C. B., Norris, D. J. & Bawendi, M. G. Synthesis and characterization of nearly monodisperse CdE (E = S, Se, Te) semiconductor nanocrystallites. *J. Am. Chem. Soc.* **115,** 8706–8715 (1993).
11. Rossetti, R., Hull, R., Gibson, J. M. & Brus, L. E. Excited electronic states and optical spectra of ZnS and CdS crystallites in the ≈15 to 50 Å size range: Evolution from molecular to bulk semiconducting properties. *J. Chem. Phys.* **82,** 552–559 (1985).
12. Jenkins, R. & Snyder, R. L. *Introduction to X-ray Powder Diffractometry* (Wiley and Sons, New York, 1996).
13. Wang, Y. R. & Duke, C. B. Atomic and electronic structure of ZnS cleavage surfaces. *Phys. Rev. B* **36,** 2736–2769 (1987).
14. Raghavachari, K., Jakob, P. & Chabal, Y. J. Step relaxation and surface stress at H-terminated vicinal Si(111). *Chem. Phys. Lett.* **206,** 156–160 (1993).
15. Rühl, E. *et al.* K-shell spectroscopy of Ar gas clusters. *J. Chem. Phys.* **98,** 6820–6826 (1993).
16. Farges, J., de Feraudy, M. F., Raoult, B. & Torchet, G. Noncrystalline structure of argon clusters. II. Multilayer icosahedral structure of Ar_N clusters 50 < N < 750. *J. Phys. Chem.* **84,** 3491–3501 (1986).
17. Muilu, J. & Pakkanen, T. A. *Ab initio* study of small zinc sulfide crystallites. *Surf. Sci.* **364,** 439–452 (1996).
18. Eichkorn, K. & Ahlrichs, R. Cadmium selenide semiconductor nanocrystals: A theoretical study. *Chem. Phys. Lett.* **288,** 235–242 (1998).
19. Franceschetti, A., Fu, H., Wang, L. W. & Zunger, A. Many-body pseudopotential theory of excitons in InP and CdSe quantum dots. *Phys. Rev. B* **60,** 1819–1829 (1999).
20. Leung, K. & Whaley, K. B. Surface relaxation in CdSe nanocrystals. *J. Chem. Phys.* **110,** 11012–11022 (1999).
21. Rabani, E. Structure and electrostatic properties of passivated CdSe nanocrystals. *J. Chem. Phys.* **115,** 1493–1497 (2001).

22. McGinley, C. *et al.* Evidence for surface reconstruction on InAs nanocrystals. *Phys. Rev. B* **65,** 245308 (2002).

23. Meulenberg, R. W. & Strouse, G. F. Vibrational analysis of nanocrystal CdSe surfaces: Evidence for surface reconstruction. *Abstr. Pap. Am. Chem. Soc.* **220,** 404-Phys (2000).

24. Hertl, W. Surface chemical properties of zinc sulfide. *Langmuir* **4,** 594–598 (1988).

25. Rockenburger, J. *et al.* The contributions of particle core and surface to strain, disorder and vibrations in thiolcapped CdTe nanocrystals. *J. Chem. Phys.* **108,** 7807–7815 (1998).

26. Head-Gordon, T. & Hura, G. Water structure from scattering experiments and simulation. *Chem. Rev.* **102,** 2651–2670 (2002).

27. Guinier, A. *X-Ray Diffraction in Crystals, Imperfect Crystals and Amorphous Bodies* (Freeman & Co., San Francisco, 1963).

28. Wright, K. & Jackson, R. A. Computer simulations of the structure and defect properties of zinc sulfide. *J. Mater. Chem.* **5,** 2037–2040 (1995).

29. Desgreniers, S., Beaulieu, L. & Leparge, I. Pressure-induced structural changes in ZnS. *Phys. Rev. B* **61,** 8726–8733 (2000).

30. de Leeuw, N. H. & Parker, S. C. Molecular-dynamics simulation of MgO surfaces in liquid water using a shell-model potential for water. *Phys. Rev. B* **58,** 13901–13908 (1998).

31. Berendsen, H. J. C., Grigera, J. R. & Straatsma, T. P. The missing term in effective pair potentials. *J. Phys. Chem.* **91,** 6269–6271 (1987).

32. Stillinger, F. H. & Rahman, A. Revised central force potentials for water. *J. Chem. Phys.* **68,** 666–670 (1978).

33. Harris, D. J., Brodholt, J. P., Harding, J. H. & Sherman, D. M. Molecular dynamics simulation of aqueous $ZnCl_2$ solutions. *Mol. Phys.* **99,** 825–833 (2001).

34. Stevens, J. E., Chaudhuri, R. K. & Freed, K. F. Global three-dimensional potential energy surfaces of H_2S from the *ab initio* effective valence shell Hamiltonian method. *J. Chem. Phys.* **105,** 8754–8768 (1996).

Controlling molecular deposition and layer structure with supramolecular surface assemblies

James A. Theobald[1], **Neil S. Oxtoby**[2], **Michael A. Phillips**[1], **Neil R. Champness**[2] & **Peter H. Beton**[1]

[1]*School of Physics and Astronomy,* [2]*School of Chemistry, University of Nottingham, Nottingham NG7 2RD, UK*

Selective non-covalent interactions have been widely exploited in solution-based chemistry to direct the assembly of molecules into nanometre-sized functional structures such as capsules, switches and prototype machines[1–5]. More recently, the concepts of supramolecular organization have also been applied to two-dimensional assemblies on surfaces[6,7] stabilized by hydrogen bonding[8–14], dipolar coupling[15–17] or metal co-ordination[18]. Structures realized to date include isolated rows[8,13–15], clusters[9,10,18] and extended networks[10–12,17], as well as more complex multi-component arrangements[16]. Another approach to controlling surface structures uses adsorbed molecular monolayers to create preferential binding sites that accommodate individual target molecules[19,20]. Here we combine these approaches, by using hydrogen bonding to guide the assembly of two types of molecules into a two-dimensional open honeycomb network that

then controls and templates new surface phases formed by subsequently deposited fullerene molecules. We find that the open network acts as a two-dimensional array of large pores of sufficient capacity to accommodate several large guest molecules, with the network itself also serving as a template for the formation of a fullerene layer.

We investigate an open honeycomb network formed when perylene tetra-carboxylic di-imide (PTCDI; Fig. 1a) is co-adsorbed with melamine (1,3,5-triazine-2,4,6-triamine; Fig. 1b) on a silver-terminated silicon surface. Melamine, which has a three-fold symmetry, forms the vertices of the network while the straight edges correspond to PTCDI. The network is stabilized by melamine–PTCDI hydrogen bonding. Melamine and PTCDI were chosen for this application because they are expected to exhibit much stronger hetero- as opposed to homo-molecular hydrogen bonding. As shown in Fig. 1, the compatibility of molecular geometries results in three hydrogen bonds per melamine–PTCDI pair, as compared
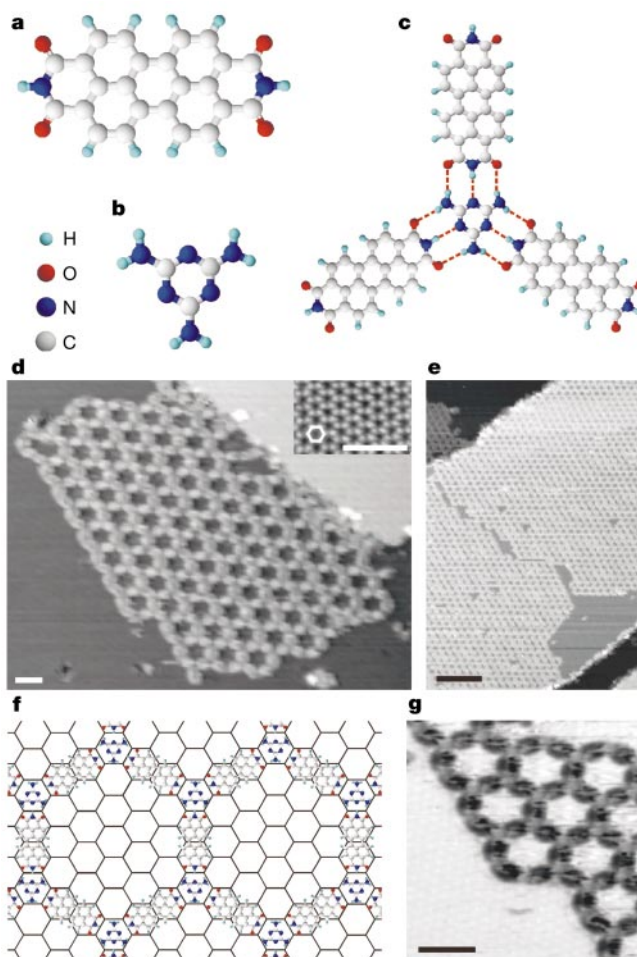
Figure 1 Self-assembly of a PTCDI–melamine supramolecular network. **a**, **b**, Chemical structure of PTCDI (**a**) and melamine (**b**). **c**, Schematic diagram of a PTCDI–melamine junction. Dotted lines represent the stabilizing hydrogen bonds between the molecules. **d**, STM image of a PTCDI–melamine network (sample voltage −2 V, tunnel current 0.1 nA). Inset, high-resolution view of the Ag/Si(111)-$\sqrt{3} \times \sqrt{3}$R30° substrate surface; the vertices and centres of hexagons correspond, respectively, to the bright (Ag trimers) and dark (Si trimers) topographic features in the STM image (surface lattice constant, $a_0 = 6.65$ Å; ref. 22). Scale bars, 3 nm. **e**, STM image of large-area network, with domains extending across terraces on the Ag/Si(111)-$\sqrt{3} \times \sqrt{3}$R30° surface (−2 V, 0.1 nA). Scale bar, 20 nm. **f**, Schematic diagram showing the registry of the network with the surface. **g**, Inverted contrast image (−2 V, 0.1 nA) of the network. Scale bar, 3 nm.